

Chiral cat state generation via the Sagnac-Fizeau effect

Yu-Hong Liu,¹ Xian-Li Yin,¹ Hui Jing,¹ Le-Man Kuang,¹ and Jie-Qiao Liao^{1,2,*}

¹*Key Laboratory of Low-Dimensional Quantum Structures and Quantum Control of Ministry of Education, Key Laboratory for Matter Microstructure and Function of Hunan Province, Department of Physics and Synergetic Innovation Center for Quantum Effects and Applications, Hunan Normal University, Changsha, 410081, China*

²*Institute of Interdisciplinary Studies, Hunan Normal University, Changsha, 410081, China*

(Dated: August 27, 2024)

The Schrödinger cat states are a kind of significant quantum resource in quantum physics and quantum information science. Here we propose a proposal for generating chiral cat states in a spinning resonator supporting both the clockwise (CW) and counterclockwise (CCW) traveling modes, which are dispersively coupled to a two-level atom. The physical mechanism for the chiral cat-state generation is based on the Sagnac-Fizeau effect. Concretely, when the resonator is rotating, the CW and CCW modes have different frequency detuning with respect to the atomic transition frequency, and hence the atomic-state-dependent rotating angular velocities for the CW and CCW modes in phase space are different. This mode-dependent evolution leads to the chirality in the state generation. By choosing proper system parameters, we achieve the separate generation of the Schrödinger cat states and coherent states in the two traveling modes. We also investigate quantum coherence properties of the generated states by examining their Wigner functions. In addition, the influence of the system dissipations on the state generation in the open-system case is investigated. Our work will provide some insights into the development of chiral optical devices and nonreciprocal photonics physics.

I. INTRODUCTION

The Schrödinger cat states are an essential resource for studying fundamental quantum physics [1, 2], including exploring macroscopic quantum coherence [3, 4], quantum decoherence [5–7], and quantum-classical boundary [8, 9]. They also have wide application potential in quantum information processing, such as quantum teleportation [10–12], quantum communication [13–16], quantum computation [17–22], and quantum precision measurement [23–25]. So far, various methods have been proposed to create the Schrödinger cat states, including conditional rotation mechanism [16, 26, 27], conditional displacement mechanism [28–34], non-Gaussian measurement [35–40], quantum state transfer [41, 42], Kerr-nonlinear evolution [43–48], and reservoir engineering techniques [49–51]. However, most previous schemes have seldomly focused on designing the cat states with directional differences [52], making them less suitable for nonreciprocal applications such as nonreciprocal quantum communications [53, 54], chiral optical devices [52, 55–57], and stable codes for quantum error correction [58, 59]. As a result, how to create chiral cat states remains an interesting and desired topic in quantum physics and quantum optics.

Quantum nonreciprocal devices are fundamental components in chiral quantum technologies, and much recent attention has been paid to nonreciprocal physics [55, 60–66]. Spinning resonators, which exhibit the broken time-reversal symmetry, provide an ideal platform for realizing nonreciprocal devices [67–69]. Recently, some

significant progress has been achieved based on spinning resonators, including nonreciprocal photon blockade [70], nonreciprocal entanglement [62, 71], and nonreciprocal topological phonon transfer [72]. However, the in-depth exploration of chirality-related mechanisms in spinning resonators, particularly the controlled generation and manipulation of chiral quantum states, remains an ongoing challenge. Addressing these issues is crucial for both understanding and practical applications of chiral quantum technologies. Note that the nonreciprocal generation of the Schrödinger cat states induced by the topological effect has been theoretically studied. [73].

Inspired by both the Schrödinger-cat-state generation via the dispersive Jaynes-Cummings model [27] and the Sagnac-Fizeau effect [67], we propose an approach for creating chiral cat states in a system comprising a two-level atom coupled to a spinning resonator, which supports both clockwise (CW) and counterclockwise (CCW) traveling modes. The rotation of the resonator induces a Sagnac-Fizeau effect, resulting in different effective frequencies for the CW and CCW modes relative to the atomic frequency. The effective differences in frequency detunings of the CW and CCW modes induce distinct quantum state generation for the two traveling modes. Concretely, by adjusting the system parameters, we prepare a coherent state in one of the traveling modes and a cat state in the other one. We investigate the coherence properties of these generated states by examining their Wigner functions. We also consider the influence of the system dissipations on the state generation. Our proposal paves the way for developing quantum chiral devices based on the coupled atom-cavity systems.

The rest of this paper is organized as follows. In

* Corresponding author: jqiao@hunnu.edu.cn

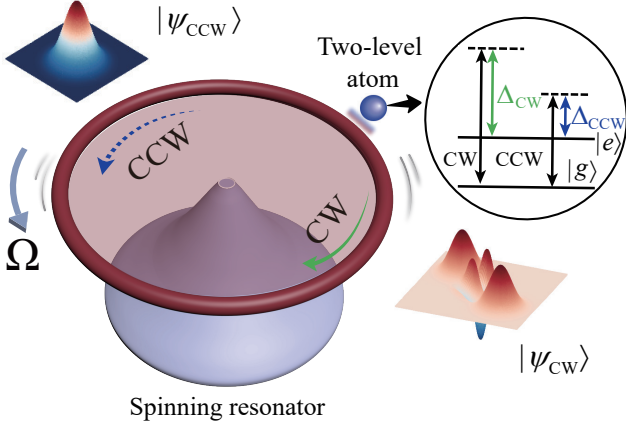


FIG. 1. Schematic of the cavity-QED system consisting of a two-level atom coupled to a spinning resonator via the optical evanescent fields. The spinning resonator supports both the clockwise (CW) and counterclockwise (CCW) traveling modes, denoted as a_{CW} and a_{CCW} , respectively. The two cavity modes are initially prepared in coherent states. By rotating the resonator along the CCW direction at an angular velocity Ω , the effective frequency for the CW (CCW) traveling mode experienced by the atom becomes $\omega_c + \Delta_{\text{sag}}$ ($\omega_c - \Delta_{\text{sag}}$), where ω_c is the nonspinning resonance frequency of the resonator and Δ_{sag} is the rotation-induced Sagnac-Fizeau frequency shift.

Sec. II, we introduce the physical model and derive the effective Hamiltonians. In Sec. III, we investigate the generation of chiral cat states and analyze the nonclassical properties of these generated states by examining their Wigner functions. We also numerically calculate the exact state generation and verify the validity of the approximation with the fidelity. In Sec. IV, we present numerical simulations of the state generation in the open-system case, and investigate the influence of the system dissipations on the state generation. Finally, we discuss the experimental implementation of this scheme and conclude this work in Sec. V.

II. PHYSICAL MODEL AND HAMILTONIANS

We consider a cavity-QED system consisting of a two-level atom with an energy separation ω_a coupled to a spinning resonator supporting both the CW and CCW traveling modes via the optical evanescent fields (Fig. 1). The rotation of the resonator in the CCW direction at an angular velocity Ω induces a Sagnac-Fizeau frequency shift for both the CW and CCW modes. Then the effective frequencies of the CW and CCW modes become $\omega_c + \Delta_{\text{sag}}$ and $\omega_c - \Delta_{\text{sag}}$, respectively. Here, ω_c is the resonance frequency of the stationary resonator, and Δ_{sag} is the Sagnac-Fizeau frequency shift defined as [67]

$$\Delta_{\text{sag}} = \frac{n_r R \Omega \omega_c}{c} \left(1 - \frac{1}{n_r^2} - \frac{\lambda}{n_r} \frac{dn_r}{d\lambda} \right). \quad (1)$$

In Eq. (1), λ and c represent the wavelength of the field mode and the speed of light in vacuum, respectively, n_r is the refractive index, and R is the radius of the resonator. The term $dn_r/d\lambda$ is the dispersion term related to the relativistic origin of the Sagnac effect, which is relatively small and can be ignored in typical materials [67, 68].

In a rotating frame defined by the unitary operator $\exp[-i\omega_a(\sigma_z/2 + a_{CW}^\dagger a_{CW} + a_{CCW}^\dagger a_{CCW})t]$, the Hamiltonian of the system can be written as ($\hbar = 1$)

$$H = \sum_{\epsilon=CW,CCW} [\Delta_\epsilon a_\epsilon^\dagger a_\epsilon + J(a_\epsilon^\dagger \sigma_- + a_\epsilon \sigma_+)], \quad (2)$$

where $\sigma_z \equiv |e\rangle\langle e| - |g\rangle\langle g|$ is z -direction Pauli operator, with $|g\rangle$ and $|e\rangle$ being the ground and excited states of the two-level atom, respectively. The operators $\sigma_- \equiv |g\rangle\langle e|$ and $\sigma_+ \equiv |e\rangle\langle g|$ are, respectively, the lowering and raising operators of the atom. The operators a_ϵ^\dagger and a_ϵ ($\epsilon = CW, CCW$) are the creation and annihilation operators of the ϵ mode. The variables $\Delta_{CW} \equiv \Delta + \Delta_{\text{sag}}$ and $\Delta_{CCW} \equiv \Delta - \Delta_{\text{sag}}$ represent, respectively, the effective frequency detunings of the CW and CCW modes with respect to the resonance frequency of the atom, with $\Delta \equiv \omega_c - \omega_a$. The parameter J denotes the coupling strength between the two traveling modes and the atom.

In this work, we consider the dispersive regime of the cavity-field-atom couplings, namely, the detunings between the two-level atom and the cavity field are much larger than the coupling strengths, i.e., $\Delta_{\epsilon=CW,CCW} \gg J\sqrt{n_\epsilon + 1}$ [74], where n_ϵ are the maximally involved photon numbers in the two cavity modes. In this case, we can perform the Frohlich-Nakajima transformation [75, 76] on the Hamiltonian (2) to derive the effective Hamiltonian by eliminating the coherent transitions between the two atomic states,

$$\begin{aligned} H_S &= e^{-S} H e^S \\ &\approx \sum_{\epsilon=CW,CCW} (\Delta_\epsilon a_\epsilon^\dagger a_\epsilon - \zeta_\epsilon a_\epsilon^\dagger a_\epsilon \sigma_z - \zeta_\epsilon \sigma_z / 2) \\ &\quad - \frac{1}{2} (\zeta_{CW} + \zeta_{CCW}) (a_{CW}^\dagger a_{CCW} + a_{CCW}^\dagger a_{CW}) \sigma_z, \end{aligned} \quad (3)$$

where $S = \sum_{\epsilon=CW,CCW} (J/\Delta_\epsilon) (a_\epsilon \sigma_+ - a_\epsilon^\dagger \sigma_-)$ with $\zeta_\epsilon = J^2/\Delta_\epsilon$. Under the parameter condition

$$\zeta_{\epsilon=CW,CCW} / 4\Delta_{\text{sag}} \ll 1, \quad (4)$$

we can discard approximately the excitation-exchange interaction term between the two traveling modes and obtain the approximate Hamiltonian

$$H_{\text{app}} = \sum_{\epsilon=CW,CCW} (\Delta_\epsilon a_\epsilon^\dagger a_\epsilon - \zeta_\epsilon a_\epsilon^\dagger a_\epsilon \sigma_z - \zeta_\epsilon \sigma_z / 2). \quad (5)$$

The physical mechanism of the chiral cat-state generation can be understood more clearly by expressing the approximate Hamiltonian of the system in the form

of conditional rotation couplings

$$H_{\text{app}} = \sum_{\epsilon=\text{CW,CCW}} [\Delta_{\epsilon} a_{\epsilon}^{\dagger} a_{\epsilon} - \zeta_{\epsilon} (a_{\epsilon}^{\dagger} a_{\epsilon} + 1/2) |e\rangle\langle e| + \zeta_{\epsilon} (a_{\epsilon}^{\dagger} a_{\epsilon} + 1/2) |g\rangle\langle g|]. \quad (6)$$

Here, the opposite signs of the coefficients for $|e\rangle\langle e|$ and $|g\rangle\langle g|$ can be used to generate cat states for the traveling modes, and the different values of ζ_{CW} and ζ_{CCW} lead to different phase space positions for the two traveling modes, since the effective rotating velocities of the two modes are different.

III. GENERATION OF THE CHIRAL CAT STATES

In this section, we explore the generation of chiral cat states based on the approximate Hamiltonian H_{app} in Eq. (5). To investigate the quantum coherence effect of the generated chiral cat states, we examine the Wigner function of the generate states. To evaluate the validity of the approximation, additionally, we derive the exact states governed by the full Hamiltonian (2) and evaluate the fidelities between the approximate states and the exact states.

A. Analytical results of the chiral cat states and their Wigner functions governed by the approximate Hamiltonian H_{app}

The unitary evolution operator associated with the approximate Hamiltonian H_{app} is given by $U_{\text{app}}(t) = \exp(-iH_{\text{app}}t)$. To generate the chiral cat states, we assume that the system is initially prepared in the state

$$|\psi_{\text{app}}(0)\rangle = \frac{1}{\sqrt{2}} (|g\rangle + |e\rangle) |\alpha\rangle_{\text{CW}} |\alpha\rangle_{\text{CCW}}, \quad (7)$$

where $|\alpha\rangle_{\text{CW}}$ and $|\alpha\rangle_{\text{CCW}}$ denote the coherent states of the CW and CCW modes, respectively. The state of the system at time t can be obtained as

$$|\psi_{\text{app}}(t)\rangle = \frac{1}{\sqrt{2}} [e^{-i\vartheta(t)} |g\rangle |\alpha_{\text{CW}}^{(+)}(t)\rangle_{\text{CW}} |\alpha_{\text{CCW}}^{(+)}(t)\rangle_{\text{CCW}} + e^{i\vartheta(t)} |e\rangle |\alpha_{\text{CW}}^{(-)}(t)\rangle_{\text{CW}} |\alpha_{\text{CCW}}^{(-)}(t)\rangle_{\text{CCW}}], \quad (8)$$

where we introduce the phase factor $\vartheta(t) = (\zeta_{\text{CW}} + \zeta_{\text{CCW}})t/2$ and the displacement amplitudes $\alpha_{\epsilon=\text{CW,CCW}}^{(\pm)}(t) = \alpha e^{-i(\Delta_{\epsilon} \pm \zeta_{\epsilon})t}$ for the CW and CCW modes. The values of these coherent state amplitudes $\alpha_{\text{CW}}^{(\pm)}(t)$ and $\alpha_{\text{CCW}}^{(\pm)}(t)$ are crucial for the generation of the chiral cat states. Specifically, for the same mode (denoted by the same subscripts), the difference between $\alpha^{(+)}(t)$ and $\alpha^{(-)}(t)$ promotes the generation of the cat states. Conversely, when the superscripts are identical, the variation in amplitudes between the CW and CCW

modes induces the evolution of distinct quantum states, thereby driving the dynamics of the chiral cat states.

To generate quantum superposed states of the traveling modes, we measure the state of the atom using the basis states $|\pm\rangle = (|e\rangle \pm |g\rangle)/\sqrt{2}$. By expressing the atomic state with the bases $|\pm\rangle$, the generated state $|\psi_{\text{app}}(t)\rangle$ can be re-expressed as

$$|\psi_{\text{app}}(t)\rangle = \frac{1}{2\mathcal{M}_{+}(t)} |+\rangle |\psi_{+}(t)\rangle + \frac{1}{2\mathcal{M}_{-}(t)} |-\rangle |\psi_{-}(t)\rangle, \quad (9)$$

where we introduce

$$|\psi_{\pm}(t)\rangle = \mathcal{M}_{\pm}(t) [e^{i\vartheta(t)} |\alpha_{\text{CW}}^{(-)}(t)\rangle_{\text{CW}} |\alpha_{\text{CCW}}^{(-)}(t)\rangle_{\text{CCW}} \pm e^{-i\vartheta(t)} |\alpha_{\text{CW}}^{(+)}(t)\rangle_{\text{CW}} |\alpha_{\text{CCW}}^{(+)}(t)\rangle_{\text{CCW}}], \quad (10)$$

with the normalization coefficients

$$\mathcal{M}_{\pm}(t) = \left[2 \pm \sum_{l=1,-1} \exp \left[2li\vartheta(t) + |\alpha|^2 \right] \times \left(\sum_{\epsilon=\text{cw,ccw}} \exp(2li\zeta_{\epsilon}t) - 2 \right) \right]^{-\frac{1}{2}}. \quad (11)$$

The measurement probabilities corresponding to the detected atomic states $|\pm\rangle$ are

$$\mathcal{P}_{\pm}(t) = \frac{1}{4} \left[2 \pm \sum_{l=1,-1} \exp \left[2li\vartheta(t) + |\alpha|^2 \right] \times \left(\sum_{\epsilon=\text{cw,ccw}} \exp(2li\zeta_{\epsilon}t) - 2 \right) \right]. \quad (12)$$

We will compare these probabilities given in Eq. (12) with those results corresponding to the exact state case in the next subsection.

Typically, the states $|\psi_{\pm}(t)\rangle$ of the CW and CCW modes are entangled states. However, when the two coherent state amplitudes for one of the two modes are overlapped, i.e., $\alpha_{\text{CW/CCW}}^{(+)} = \alpha_{\text{CW/CCW}}^{(-)}$, then the two modes will be disentangled. For example, we set the effective detunings $\Delta_{\text{CW}} = 2\Delta_{\text{CCW}}$, then the CW mode is in a maximally distinguishable coherent state (cat state) while the CCW mode can remain in a coherent state at time $t_s = \pi/2\zeta_{\text{CW}}$. We denote this phenomenon as the generation of chiral cat states, i.e., creating distinct states in the two different rotating modes of the cavity. When $\Delta_{\text{CW}} \neq 2\Delta_{\text{CCW}}$, it becomes impossible to simultaneously achieve a coherent state and a maximally distinguishable cat state. In this case, one mode is in a coherent state while the other mode is in a less distinguishable cat state. Nonetheless, a chiral cat state can still be generated under these conditions.

To demonstrate the quantum coherence effect in the generated chiral cat states, we calculate the Wigner function [77] for both the CW and CCW modes. When the CW and CCW modes are in the states described

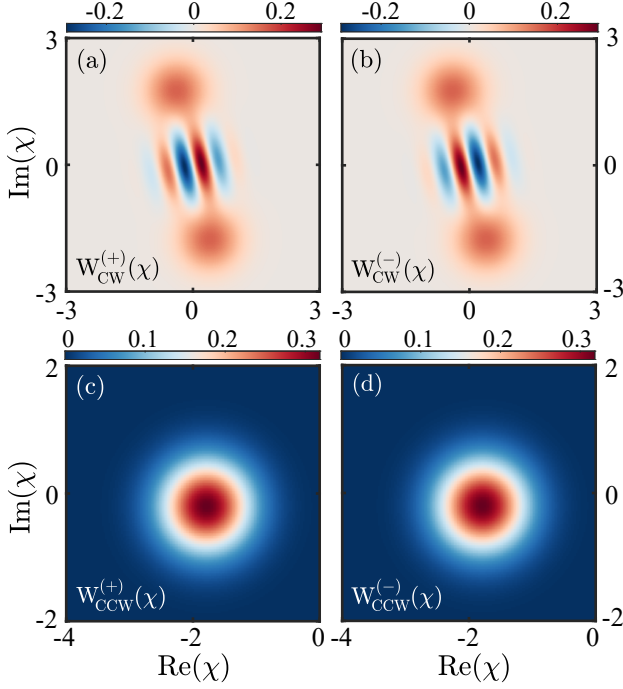


FIG. 2. The Wigner functions $W_{\text{CW,CCW}}^{(\pm)}(\chi)$ of the generated states $\rho_{\text{CW,CCW}}^{(\pm)}$ at time $t_s = \pi/2\zeta_{\text{CW}}$. Panels (a) and (b) [(c) and (d)] show the Wigner functions $W_{\text{CW}}^{(+)}(\chi)$ and $W_{\text{CW}}^{(-)}(\chi)$ [$W_{\text{CCW}}^{(+)}(\chi)$ and $W_{\text{CCW}}^{(-)}(\chi)$] for the CW (CCW) mode, respectively. The coherent amplitude of the initial coherent state $|\alpha\rangle$ is $\alpha = 1.8$. Other parameters used are $\Delta/J = 33$ and $\Delta_{\text{sag}}/J = 11$.

by the density matrices ρ_{CW} and ρ_{CCW} , respectively, the Wigner functions are defined by

$$W_{\epsilon=\text{CW,CCW}}(\chi) = \frac{2}{\pi} \text{Tr}[D_{\epsilon}^{\dagger}(\chi)\rho_{\epsilon}D_{\epsilon}(\chi)(-1)^{a_{\epsilon}^{\dagger}a_{\epsilon}}], \quad (13)$$

where $D_{\epsilon}(\chi) = \exp(\chi a_{\epsilon}^{\dagger} - \chi^* a_{\epsilon})$ is the displacement operator. For the states given in Eq. (10), we take the outer product $\rho^{(\pm)} = |\psi_{\pm}(t)\rangle\langle\psi_{\pm}(t)|$ and trace out one of the modes to obtain $\rho_{\bar{\epsilon}}^{(\pm)} = \text{Tr}_{\epsilon}(\rho^{(\pm)})$, where $\bar{\epsilon}$ denotes the complement of ϵ , i.e., $\overline{\text{CW}} = \text{CCW}$ and $\overline{\text{CCW}} = \text{CW}$. In terms of these reduced density matrices, the Wigner functions $W_{\text{CW,CCW}}^{(\pm)}(\chi)$ can be obtained as

$$W_{\epsilon=\text{CW,CCW}}^{(\pm)}(\chi) = \frac{2|\mathcal{M}_{\pm}|^2}{\pi} [\Lambda_{\epsilon}^{(1)}(\chi) \pm \Lambda_{\epsilon}^{(2)}(\chi) \pm \Lambda_{\epsilon}^{(3)}(\chi) + \Lambda_{\epsilon}^{(4)}(\chi)], \quad (14)$$

where we introduce

$$\Lambda_{\epsilon}^{(1)}(\chi) = \exp[2[\alpha_{\epsilon}^{(+)}(t)]^* \chi + 2\chi^* \alpha_{\epsilon}^{(+)}(t) - 2|\alpha|^2 - 2|\chi|^2], \quad (15a)$$

$$\Lambda_{\epsilon}^{(2)}(\chi) = \exp[-2i\vartheta(t) + |\alpha|^2(e^{-2i\zeta_{\epsilon}t} - e^{-2i\zeta_{\bar{\epsilon}}t} - 2) + 2\chi[\alpha_{\epsilon}^{(-)}(t)]^* + 2\chi^* \alpha_{\epsilon}^{(+)}(t) - 2|\chi|^2], \quad (15b)$$

$$\Lambda_{\epsilon}^{(3)}(\chi) = \exp[2i\vartheta(t) + |\alpha|^2(e^{2i\zeta_{\epsilon}t} - e^{2i\zeta_{\bar{\epsilon}}t} - 2) + 2\chi[\alpha_{\epsilon}^{(+)}(t)]^* + 2\chi^* \alpha_{\epsilon}^{(-)}(t) - 2|\chi|^2], \quad (15c)$$

$$\Lambda_{\epsilon}^{(4)}(\chi) = \exp[2[\alpha_{\epsilon}^{(-)}(t)]^* \chi + 2\chi^* \alpha_{\epsilon}^{(-)}(t) - 2|\alpha|^2 - 2|\chi|^2]. \quad (15d)$$

In Figs. 2(a)-2(d), we show the Wigner functions $W_{\text{CW,CCW}}^{(\pm)}(\chi)$ for both the CW and CCW modes at time $t_s = \pi/2\zeta_{\text{CW}} = 69.11J^{-1}$. Concretely, Figs. 2(a) and 2(b) display the Wigner functions $W_{\text{CW}}^{(+)}(\chi)$ and $W_{\text{CW}}^{(-)}(\chi)$ for the CW mode, respectively. Here we can see distinct interference fringes caused by quantum superposition of two coherent states. The interference fringes indicate the presence of coherent superposition states, commonly referred to as cat states. In contrast, the Wigner functions for the CCW mode exhibiting Gaussian peaks in the phase space, as shown in Figs. 2(c) and 2(d), which are signature for coherent states in the CCW mode. We note that the appearance of the coherent state for the CCW mode is caused by the overlap between the two coherent amplitudes $\alpha_{\text{CCW}}^{(-)}(t_s)$ and $\alpha_{\text{CCW}}^{(+)}(t_s)$. Comparing Figs. 2(a) [2(b)] with 2(c) [2(d)], we observe that the CW mode is in a cat state while the CCW mode is in a coherent state, demonstrating the generation of chiral cat states.

B. Exact states determined by the full Hamiltonian H and the fidelities between the exact and approximate states

In the above section, we have calculated the generated states governed by the approximate Hamiltonian. To evaluate the state generation in a realistic case, we need to calculate the state generation with the full Hamiltonian, and evaluate the fidelity between the approximate and exact states. The exact state of this system can be determined by numerically solving the Schrödinger equation with the full Hamiltonian (2). For the present system, a general pure state can be expressed as

$$|\Psi(t)\rangle = \sum_{m,k=0}^{\infty} [A_{m,k}(t)|e\rangle|m\rangle_{\text{CW}}|k\rangle_{\text{CCW}} + B_{m,k}(t)|g\rangle|m\rangle_{\text{CW}}|k\rangle_{\text{CCW}}], \quad (16)$$

where $|m\rangle_{\text{CW}}$ and $|k\rangle_{\text{CCW}}$ represent the Fock states of the CW and CCW modes, respectively. $A_{m,k}(t)$ and $B_{m,k}(t)$ are the probability amplitudes. By substituting Eq. (2) and Eq. (16) into the Schrödinger equation, we derive

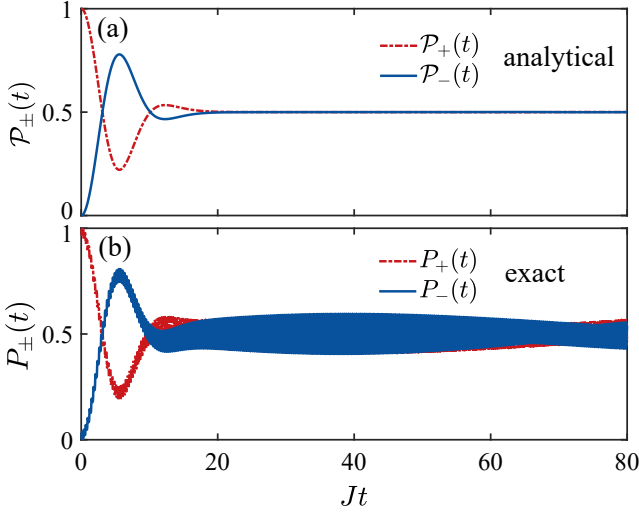


FIG. 3. The analytical measurement probabilities $\mathcal{P}_\pm(t)$ (a) from Eq. (12) and the exact measurement probabilities $P_\pm(t)$ (b) from Eq. (19) as functions of the scaled evolution time Jt . For the exact solution in panel (b), both the CW and CCW modes have a truncation dimension of 13. Other parameters used in panels (a) and (b) are the same as those in Fig. 2.

the equations of motion for the probability amplitudes $A_{m,k}(t)$ and $B_{m,k}(t)$ as

$$\dot{A}_{m,k}(t) = -i(m\Delta_{\text{CW}} + k\Delta_{\text{CCW}})A_{m,k}(t) - iJ\sqrt{m+1} \times B_{m+1,k}(t) - iJ\sqrt{k+1}B_{m,k+1}(t), \quad (17a)$$

$$\dot{B}_{m,k}(t) = -i(m\Delta_{\text{CW}} + k\Delta_{\text{CCW}})B_{m,k}(t) - iJ\sqrt{m} \times A_{m-1,k}(t) - iJ\sqrt{k}A_{m,k-1}(t). \quad (17b)$$

For the initial state $|+\rangle|\alpha\rangle_{\text{CW}}|\alpha\rangle_{\text{CCW}}$, the initial conditions for the probability amplitudes are $A_{m,k}(0) = B_{m,k}(0) = e^{-|\alpha|^2}\alpha^{m+k}/\sqrt{2m!k!}$. Using these initial conditions, the evolution of the probability amplitudes $A_{m,k}(t)$ and $B_{m,k}(t)$ can be obtained by numerically solving Eqs. (17a) and (17b), then the exact state of the system is obtained.

When the atom is detected in the states $|\pm\rangle$, the CW and CCW modes collapse into the corresponding states

$$|\Psi_\pm(t)\rangle = \frac{1}{\sqrt{2P_\pm(t)}} \sum_{m,k=0}^{\infty} [A_{m,k}(t) \pm B_{m,k}(t)] |m\rangle_{\text{CW}} |k\rangle_{\text{CCW}}, \quad (18)$$

with the corresponding detection probabilities

$$P_\pm(t) = \frac{1}{2} \sum_{m,k=0}^{\infty} |[A_{m,k}(t) \pm B_{m,k}(t)]|^2. \quad (19)$$

In Fig. 3(a), we display the analytical measurement probabilities $\mathcal{P}_\pm(t)$, given by Eq. (12), vs the scaled evolution time Jt . We observe that the sum of $\mathcal{P}_+(t)$ and $\mathcal{P}_-(t)$ is normalized. Furthermore, for longer subsequent measurement time t_m , the measurement probabilities

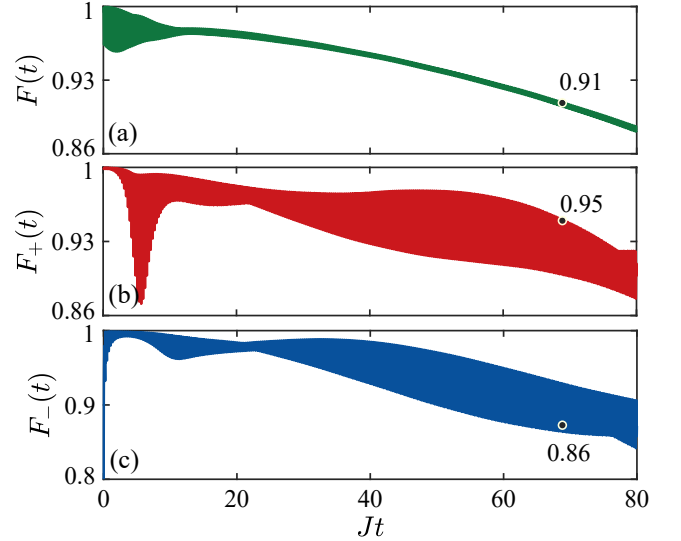


FIG. 4. The fidelities (a) $F(t)$, (b) $F_+(t)$, and (c) $F_-(t)$ as functions of the scaled evolution time Jt . The parameters used are the same as those in Fig. 2.

$\mathcal{P}_\pm(t) \approx 1/2$, corresponding to $\sum_{l=1,-1} \exp[2li\vartheta(t_m)] + |\alpha|^2 [\sum_{\epsilon=\text{CW,CCW}} \exp(2li\zeta_\epsilon t_m) - 2] \rightarrow 0$ in Eq. (12). The exact measurement probabilities $P_\pm(t)$ given by Eq. (19) are shown in Fig. 3(b). The exact measurement probabilities $P_\pm(t)$ exhibit oscillating behavior around $1/2$, which is caused by the last term in Eq. (3). By comparing the analytical results with the numerical results, we find that the analytical probability evolution is smooth, while the numerical results exhibit oscillation. Nevertheless, the pattern of the approximate and exact results agree well, which confirms the validity of the approximate made during the derivation of the approximate Hamiltonian.

To quantitatively verify the validity of the approximate Hamiltonian H_{app} , we evaluate the fidelity $F(t) = |\langle \Psi(t) | \psi_{\text{app}}(t) \rangle|^2$ between the exact and approximate states. Here, $|\psi_{\text{app}}(t)\rangle$ represents the approximate state governed by the approximate Hamiltonian H_{app} in Eq. (5), and $|\Psi(t)\rangle$ represents the exact state governed by the full Hamiltonian H in Eq. (2). Based on Eqs. (2) and (5), the fidelity can be calculated as

$$F(t) = \left| e^{-|\alpha|^2} \sum_{m,k=0}^{\infty} \left[e^{i\vartheta(t)} A_{m,k}^*(t) \frac{[\alpha_{\text{CW}}^{(-)}(t)]^m [\alpha_{\text{CCW}}^{(-)}(t)]^k}{\sqrt{2m!k!}} + e^{-i\vartheta(t)} B_{m,k}^*(t) \frac{[\alpha_{\text{CW}}^{(+)}(t)]^m [\alpha_{\text{CCW}}^{(+)}(t)]^k}{\sqrt{2m!k!}} \right] \right|^2. \quad (20)$$

Similarly, we can also evaluate the performance of the chiral cat-states generation by calculating the fidelities between the generate states $|\Psi_\pm(t)\rangle$ in Eq. (18) and the target states $|\psi_\pm(t)\rangle$ in Eq. (10). Using Eqs. (18) and (10), the fidelities $F_\pm(t) = |\langle \Psi_\pm(t) | \psi_\pm(t) \rangle|^2$ can be

obtained as

$$F_{\pm}(t) = \frac{|\mathcal{M}_{\pm}(t)|^2 e^{-2|\alpha|^2}}{P_{\pm}(t)} \left| \sum_{m,k=0}^{\infty} \left[(A_{m,k}^*(t) \pm B_{m,k}^*(t)) \times \left(e^{i\vartheta(t)} \frac{[\alpha_{\text{CW}}^{(-)}(t)]^m [\alpha_{\text{CCW}}^{(-)}(t)]^k}{\sqrt{2m!k!}} \pm e^{-i\vartheta(t)} \frac{[\alpha_{\text{CW}}^{(+)}(t)]^m [\alpha_{\text{CCW}}^{(+)}(t)]^k}{\sqrt{2m!k!}} \right) \right] \right|^2. \quad (21)$$

Figure 4 illustrates the fidelities $F(t)$ and $F_{\pm}(t)$ as functions of the scaled evolution time Jt . We observe that the fidelities $F(t)$ and $F_{\pm}(t)$ decrease gradually and exhibit oscillations over time. The decreasing fidelity over time indicates a gradual loss of correspondence between the approximate and exact states. From Figs. 4(a) to 4(c), we see that at the target moment $t_s = 69.11J^{-1}$, the fidelities $F(t_s)$, $F_+(t_s)$, and $F_-(t_s)$ take the values 0.91, 0.95, and 0.86, respectively. These relatively high fidelity values indicate that the approximate states and the exact states match well at the measurement time, demonstrating the validity of the approximation. It is worth noting that higher fidelity values can be achieved by adjusting the system parameters. However, due to the relevance between these parameters, achieving a higher fidelity usually requires a longer target time. In the open-system case, a longer evolution time will lead to a stronger cavity-photon dissipation, thereby reducing the fidelity. In realistic cases, we need to choose proper measurement time to reach a proper balance between the fidelity and the dissipation.

C. The Wigner functions of the exact states

To confirm the chiral state generation in the phase space, we calculate the Wigner functions of the exact states $|\Psi_{\pm}(t)\rangle$. Following the preceding discussions and using Eqs. (13) and (18), we derive the Wigner functions $\mathcal{W}_{\text{CW,CCW}}^{(\pm)}(\chi)$ for the exact states $|\Psi_{\pm}(t)\rangle$ as

$$\mathcal{W}_{\text{CW}}^{(\pm)}(\chi) = \frac{1}{\pi P_{\pm}(t)} \sum_{l,m,n,k=0}^{\infty} (-1)^l [A_{m,k}(t) + B_{m,k}(t)] \times [A_{n,k}^*(t) + B_{n,k}^*(t)] \mathcal{L}_{m,l}^{\text{CW}\dagger}(\chi) \mathcal{L}_{n,l}^{\text{CW}}(\chi), \quad (22a)$$

$$\mathcal{W}_{\text{CCW}}^{(\pm)}(\chi) = \frac{1}{\pi P_{\pm}(t)} \sum_{l,m,k,j=0}^{\infty} (-1)^l [A_{m,k}(t) + B_{m,k}(t)] \times [A_{m,j}^*(t) + B_{m,j}^*(t)] \mathcal{L}_{k,l}^{\text{CCW}\dagger}(\chi) \mathcal{L}_{j,l}^{\text{CCW}}(\chi). \quad (22b)$$

Here the measurement probabilities $P_{\pm}(t)$ are given by Eq. (19), and $\mathcal{L}_{n,l}^{\epsilon=\text{CW,CCW}}(\chi)$ is defined as $\mathcal{L}_{n,l}^{\epsilon}(\chi) =$

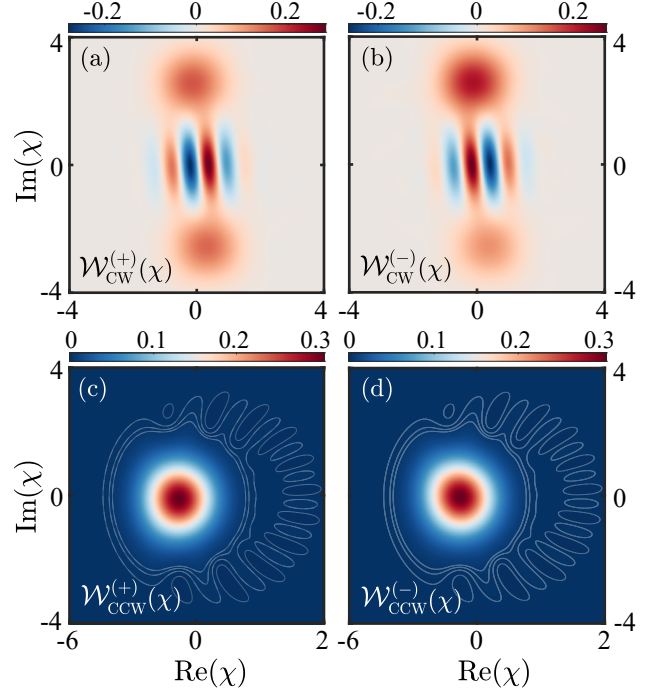


FIG. 5. (a)-(d) The Wigner functions $\mathcal{W}_{\text{CW,CCW}}^{(\pm)}(\chi)$ for the exact states $|\Psi_{\pm}(t_s)\rangle$ in Eq. (18) at time $t_s = \pi/2\zeta_{\text{CW}}$. Other parameters used are the same as those in Fig. 2.

$\epsilon \langle n | D(\chi) | l \rangle_{\epsilon}$, which is given by [78]

$$\mathcal{L}_{n,l}^{\epsilon}(\chi) = \begin{cases} \sqrt{\frac{n!}{l!}} e^{-|\chi|^2/2} (-\chi^*)^{l-n} L_n^{l-n}(|\chi|^2), & l > n, \\ \sqrt{\frac{l!}{n!}} e^{-|\chi|^2/2} (\chi)^{n-l} L_l^{n-l}(|\chi|^2), & n > l, \end{cases} \quad (23)$$

where $L_n^{l-n}(x)$ are the associated Laguerre polynomials.

In Fig. 5, we show the exact Wigner functions $\mathcal{W}_{\text{CW,CCW}}^{(\pm)}(\chi)$ at time $t_s = 69.11J^{-1}$. Figures 5(a) and 5(b) show clear interference fringes for the CW mode under the full Hamiltonian, which match well with the approximate solutions in Figs. 2(a) and 2(b). This indicates that the approximation is valid in describing the non-classical characteristics of the CW mode. For the CCW mode, however, the exact Wigner functions in Figs. 5(c) and 5(d) show small interference fringes that are not presented in the approximate solutions. These small fringes appear because the components $\alpha_{\text{CCW}}^{(-)}(t)$ and $\alpha_{\text{CCW}}^{(+)}(t)$ in phase space are not completely overlapped (the Wigner function does not form a perfectly circular Gaussian peak), resulting in some interference effects. Despite this, we can still clearly distinguish the CW and CCW modes under the full Hamiltonian, demonstrating the feasibility for generating chiral cat states with our scheme.

IV. GENERATION OF CHIRAL CAT STATES IN THE OPEN-SYSTEM CASE

In this section, we investigate the generation of chiral cat states in the open-system case. Specifically, we analyze in detail how the system dissipations affect the state-generation performance, namely, the fidelity and the state-generation probability. We also explore the influence of the dissipations on quantum coherence by calculating the Wigner functions of the generated cat states in the open-system case.

A. Quantum master equation and its exact solution

In real physical systems, the dissipations inevitably affect the dynamics of the system. For the present cavity-QED system, the average thermal excitation numbers for the cavity field and the atom are negligibly small, then we can assume that both the cavity fields and the atom are connected to individual vacuum baths. By introducing the dissipation terms for both the cavity modes and the atom, the dynamics of the system is described by the quantum master equation

$$\dot{\rho} = -i[H, \rho] + \kappa L[a_{CW}] \rho + \kappa L[a_{CCW}] \rho + \gamma L[\sigma_-] \rho, \quad (24)$$

where the Hamiltonian H is given by Eq. (2). The parameters κ and γ are the decay rates of the cavity field and the two-level atom, respectively. The superoperator $L[o]\rho = o\rho o^\dagger - (o^\dagger o\rho + \rho o^\dagger o)/2$ denotes the Lindblad term for the operators $o = a_{CW}, a_{CCW}$, and σ_- .

To solve the quantum master equation, we expand the density matrix of the system using the Fock-state bases as follows

$$\rho(t) = \sum_{w,v=e,g} \left[\sum_{m,k,n,j=0}^{\infty} \rho_{w,m,k,v,n,j}(t) \times |w\rangle|m\rangle_{CW} |k\rangle_{CCW} \langle v|_{CW} \langle n|_{CCW} \langle j| \right], \quad (25)$$

with $\rho_{w,m,k,v,n,j} = \langle w|_{CW} \langle m|_{CCW} \langle k|\rho|v\rangle_n \langle j|_{CCW}$. To numerically solve these equations of motion for the matrix density-matrix elements, we choose the initial state of the system as $|+\rangle|\alpha\rangle_{CW} |\alpha\rangle_{CCW}$, then the corresponding initial values of these density matrix elements are given by $\rho_{e,m,k,e,n,j}(0) = \rho_{g,m,k,g,n,j}(0) = \rho_{g,m,k,g,n,j}(0) = e^{-2|\alpha|^2} \alpha^{m+k} (\alpha^*)^{n+j} / 2\sqrt{m!n!k!j!}$. With the numerical solutions, we can track the evolution of the density matrix and investigate the physical properties of the generated states.

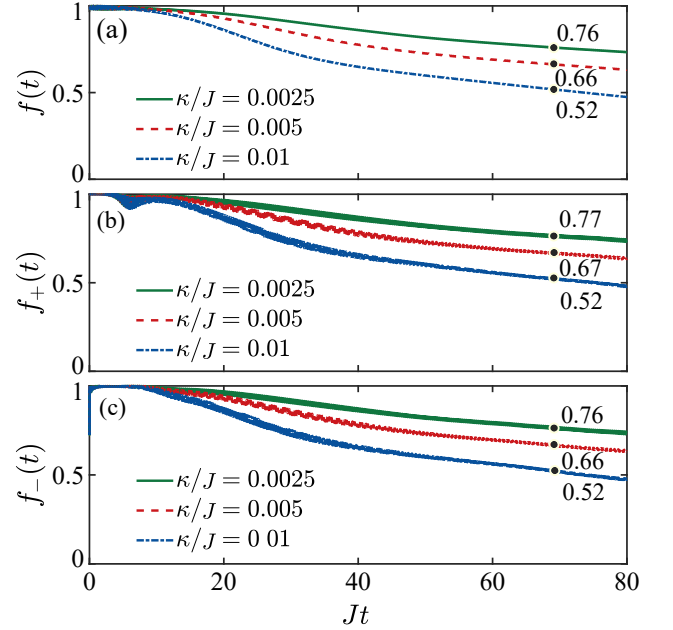


FIG. 6. The fidelities (a) $f(t)$, (b) $f_+(t)$, and (c) $f_-(t)$ as functions of the scaled evolution time Jt for different cavity-field decay rates $\kappa/J = 0.0025, 0.005$, and 0.01 . The decay rate of the atom is $\gamma/J = 0.005$. Other parameters used are the same as those in Fig. 2.

B. Fidelities between the approximate and exact states in the open-system case

To investigate the effect of the dissipations on the state generation, we calculate the fidelity $f(t) = \langle \psi(t) | \rho(t) | \psi(t) \rangle$ between the exact state $\rho(t)$ given in Eq. (25) and the analytical state $|\psi(t)\rangle$ given in Eq. (8). Particularly, for generating chiral cat states, a projective measurement upon the atomic states $|\pm\rangle$ is required. Then the corresponding density matrices for the CW and CCW modes become

$$\rho^{(\pm)}(t) = \frac{1}{2p_{\pm}(t)} \sum_{m,k,n,j} \Xi_{m,k,n,j}^{(\pm)}(t) \times |m\rangle_{CW} |k\rangle_{CCW} \langle n|_{CCW} \langle j|, \quad (26)$$

where we introduce the variables $\Xi_{m,k,n,j}^{(\pm)}(t) = \rho_{e,m,k,e,n,j}(t) + \rho_{g,m,k,g,n,j}(t) \pm \rho_{e,m,k,g,n,j}(t) \pm \rho_{g,m,k,e,n,j}(t)$, and the measurement probabilities

$$p_{\pm}(t) = \frac{1}{2} \sum_{m,k=0}^{\infty} \Xi_{m,k,m,k}^{(\pm)}(t) \quad (27)$$

corresponding to the atomic states $|\pm\rangle$. Subsequently, the fidelities $f_{\pm}(t) = \langle \psi_{\pm}(t) | \rho^{(\pm)}(t) | \psi_{\pm}(t) \rangle$ between the generated states $\rho^{(\pm)}(t)$ and the target states $|\psi_{\pm}(t)\rangle$ can be calculated accordingly.

In Fig. 6, we show the fidelities $f(t)$ and $f_{\pm}(t)$ versus the scaled evolution time Jt in the open-system

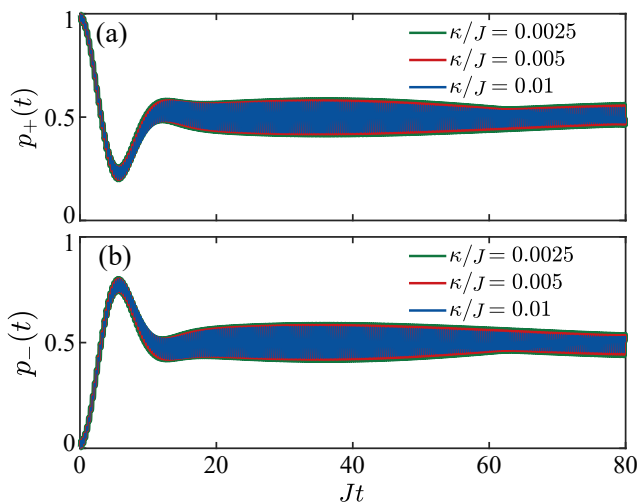


FIG. 7. The measurement probabilities (a) $p_+(t)$ and (b) $p_-(t)$ given in Eq. (27) versus the scaled evolution time Jt for different cavity-field decay rates $\kappa/J = 0.0025, 0.005,$ and 0.01 in the open-system case. The parameters used are the same as those in Fig. 6.

case. Compared to the closed-system case in Fig. 4, the presence of system dissipation accelerates the decay of the fidelities and reduces oscillations. Specifically, increasing the cavity-field decay rate from $\kappa/J = 0.0025$ to 0.005 and 0.01 leads to a more rapid fidelity reduction, as shown by the green solid, red dashed, and blue dotted curves, respectively. This trend is consistent for $f(t)$ and $f_{\pm}(t)$. Moreover, the results show that at time $t_s = 69.11J^{-1}$, the fidelities $f(t_s)$, $f_+(t_s)$, and $f_-(t_s)$ take the values $0.76, 0.77,$ and 0.76 for $\kappa/J = 0.0025$; $0.66, 0.67,$ and 0.66 for $\kappa/J = 0.005$; and $0.52, 0.52,$ and 0.52 for $\kappa/J = 0.01$, respectively. These results show that larger decay rates lead to reduced fidelity, indicating the degeneration of quantum state generation by the dissipations in the open-system case.

In Fig. 7, we show the measurement probabilities $p_+(t)$ and $p_-(t)$ versus the scaled evolution time Jt corresponding to different cavity-field decay rates in the open-system case. Both the probabilities $p_+(t)$ [Fig. 7(a)] and $p_-(t)$ [Fig. 7(b)] oscillate around 0.5 . We observe that the larger the dissipation rate is, the lower the amplitude of the oscillation envelope for the probabilities is (as depicted by the green, red, and blue curves for $\kappa/J = 0.0025, 0.005,$ and 0.01 , respectively). The reason for the reduction in the oscillation amplitude is that a stronger dissipation will cause more photons to decay, thereby reducing the impact of the last term in Eq. (3).

C. The Wigner functions of the generated states in the open-system case

In the open-system case, the dissipations of the system will reduce the quantum coherence in the generated chiral

cat states. Using Eqs. (13) and (26), we can derive the Wigner functions $\tilde{\mathcal{W}}_{\text{CW,CCW}}^{(\pm)}(\chi)$ in the open-system case as

$$\tilde{\mathcal{W}}_{\text{CW}}^{(\pm)}(\chi) = \frac{1}{\pi p_{\pm}(t)} \sum_{l,m,n,k=0}^{\infty} (-1)^l \Xi_{m,k,n,k}^{(\pm)}(t) \times \mathcal{L}_{m,l}^{\text{CW}\dagger}(\chi) \mathcal{L}_{n,l}^{\text{CW}}(\chi), \quad (28a)$$

$$\tilde{\mathcal{W}}_{\text{CCW}}^{(\pm)}(\chi) = \frac{1}{\pi p_{\pm}(t)} \sum_{l,m,j,k=0}^{\infty} (-1)^l \Xi_{m,k,m,j}^{(\pm)}(t) \times \mathcal{L}_{k,l}^{\text{CCW}\dagger}(\chi) \mathcal{L}_{j,l}^{\text{CCW}}(\chi), \quad (28b)$$

where the terms $\mathcal{L}_{n,l}^{\epsilon=\text{CW,CCW}}(\chi)$ can be calculated with Eq. (23).

In Fig. 8, we show the Wigner functions $\tilde{\mathcal{W}}_{\text{CW,CCW}}^{(\pm)}(\chi)$ of the generated states $\rho_{\epsilon=\text{CW,CCW}}^{(\pm)}$ corresponding to different cavity-field decay rates. Compared to the closed-system results in Figs. 5(a) and 5(b), we observe that increasing the cavity-field decay rate reduces quantum coherence. For both the CW and CCW modes, when the decay rate takes $\kappa/J = 0.0025$ [Figs. 8(a)-8(b)], $\kappa/J = 0.005$ [Figs. 8(e)-8(h)], and $\kappa/J = 0.01$ [Figs. 8(i)-8(l)], we find that the interference fringes in the corresponding Wigner functions become weaker for a larger κ . Despite the reduction of quantum coherence due to dissipation, the CW mode remains in a cat state, while the CCW mode remains in a coherent state. This confirms that the chiral-cat-state generation scheme is robust even in the open-system cases.

V. DISCUSSIONS AND CONCLUSION

To analyze the experimental feasibility of our scheme, we present some discussions concerning the experimental setups and the relevant parameters. Provided the use of spinning resonator, we focus on the microring resonator system coupled to a two-level system [79]. Currently, the strong coupling between a single atom and a monolithic microresonator has been observed [80, 81], with an effective coupling strength of $J/2\pi = 50 \pm 12$ MHz [80]. Moreover, the experimentally feasible parameters for the microresonator are $Q = 6.0 \times 10^9$, $R = 1.1$ mm, $n_r = 1.4$, $\lambda = 1550$ nm, and $\Omega = 6.6$ kHz [68]. These parameters result in a cavity-field decay rate $\kappa \approx 0.2$ MHz. The ratio of the cavity-field decay rate to the coupling strength used is of the same order as the experimental parameters. In our numerical simulations, the Sagnac-Fizeau frequency shift used is $\Delta_{\text{sag}} = 11J$, which corresponds to an angular velocity of $\Omega \approx \Delta_{\text{sag}}c/[n_r R \omega_c(1 - n_r^{-2})] = \Delta_{\text{sag}}\lambda/[2\pi n_r R(1 - n_r^{-2})] \approx 2\pi \times 136.9$ kHz for the above experimental parameters. We point out that this rotation angular velocity can be decreased by choosing a smaller coupling strength J . Recently, an angular velocity of 6.6 kHz has been reported. These analyses indicate that the

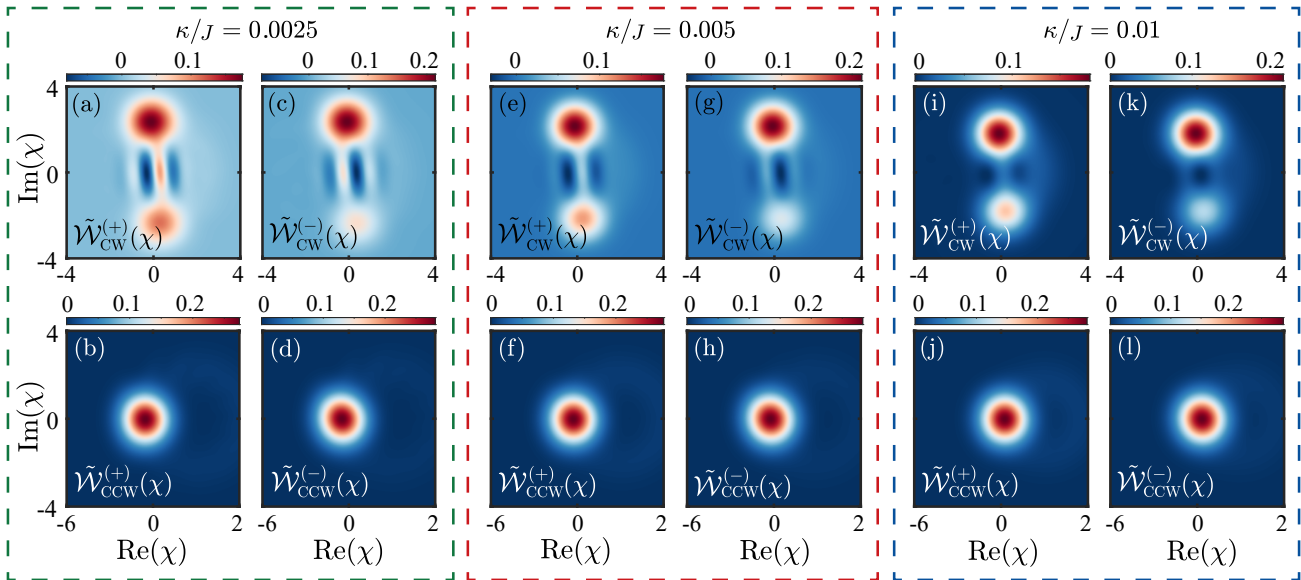


FIG. 8. The Wigner functions $\tilde{W}_{\text{CW,CCW}}^{(\pm)}(\chi)$ corresponding to the states $\rho_{\epsilon=\text{CW,CCW}}^{(\pm)} = \text{Tr}_{\epsilon}(\rho^{(\pm)})$, where $\rho^{(\pm)}$ are the states defined in Eq. (26). These Wigner functions are shown at the time $t_s = \pi/2\zeta_{\text{CW}}$ for various cavity-field decay rates: (a)-(d) $\kappa/J = 0.0025$, (e)-(h) $\kappa/J = 0.005$, and (i)-(l) $\kappa/J = 0.01$. Other parameters used are the same as those in Fig. 6.

suggested parameters should be accessible with the near future experimental technique. We also note that, even at lower angular velocities, we can still generate chiral cat states, where one mode remains in a coherent state, while the other mode is in a less distinguishable cat state.

In conclusion, we have proposed a reliable method for creating chiral cat states in a cavity-QED system consisting of a spinning resonator coupled to a two-level atom in the dispersive-coupling regime. We have shown that a cat state in the CW mode and a coherent state in the CCW mode can be successfully generated. By calculating the Wigner function, we have characterized quantum coherence properties of these generated cat states. In addition, we have examined the influence of the system dissipations on chiral cat state generation. Our work will contribute to the development of chiral quantum optics and the exploration of chiral optical devices.

ACKNOWLEDGMENTS

J.-Q.L. was supported in part by National Natural Science Foundation of China (Grants No. 12175061,

No. 12247105, No. 11935006, and No. 12421005), National Key Research and Development Program of China (Grant No. 2024YFE0102400), and Hunan Provincial Major Sci-Tech Program (Grant No. 2023ZJ1010). H.J. is supported by the Natural Science Foundation of China (NSFC) (Grant No. 11935006), the Science and Technology Innovation Program of Hunan Province (Grant No. 2020RC4047), National Key R&D Program of China (Grant No. 2024YFE0102400), and Hunan provincial major Sci-Tech program (Grant No. 2023ZJ1010). L.-M.K. is supported by the Natural Science Foundation of China (NSFC) (Grant Nos. 12247105, 12175060, 11935006, 12421005), Hunan Provincial Major Sci-Tech Program (Grant No. 2023ZJ1010), and XJ-Lab key project (Grant No. 23XJ02001). Y.-H.L. was supported in part by Hunan Provincial Postgraduate Research and Innovation project (Grant No. CX20240530).

-
- [1] E. Schrödinger, Die gegenwärtige Situation in der Quantenmechanik, *Naturwissenschaften* **23**, 807 (1935).
 [2] A. Peres, *Quantum Theory: Concepts and Methods* (Springer, Dordrecht, 2002).
 [3] A. J. Leggett and A. Garg, Quantum mechanics versus

- macroscopic realism: Is the flux there when nobody looks?, *Phys. Rev. Lett.* **54**, 857 (1985).
 [4] A. J. Leggett, Testing the limits of quantum mechanics: motivation, state of play, prospects, *J. Phys. Condens. Matter* **14**, R415 (2002).

- [5] W. H. Zurek, Decoherence, einselection, and the quantum origins of the classical, *Rev. Mod. Phys.* **75**, 715 (2003).
- [6] E. Joos, H. D. Zeh, C. Kiefer, D. J. W. Giulini, J. Kupsch and I. O. Stamatescu, *Decoherence and the Appearance of a Classical World in Quantum Theory* (Springer, Berlin, 2013).
- [7] M. Brune, E. Hagley, J. Dreyer, X. Maître, A. Maali, C. Wunderlich, J. M. Raimond, and S. Haroche, Observing the Progressive Decoherence of the “Meter” in a Quantum Measurement, *Phys. Rev. Lett.* **77**, 4887 (1996).
- [8] W. H. Zurek, Decoherence and the Transition from Quantum to Classical, *Phys. Today* **44**(10), 36 (1991).
- [9] S. Haroche, Nobel lecture: Controlling photons in a box and exploring the quantum to classical boundary, *Rev. Mod. Phys.* **85**, 1083 (2013).
- [10] S. L. Braunstein and H. J. Kimble, Teleportation of Continuous Quantum Variables, *Phys. Rev. Lett.* **80**, 869 (1998).
- [11] A. Furusawa, J. L. Sørensen, S. L. Braunstein, C. A. Fuchs, H. J. Kimble, and E. S. Polzik, Unconditional Quantum Teleportation, *Science* **282**, 706 (1998).
- [12] J.-Q. Liao and L.-M. Kuang, A new optical scheme for quantum teleportation of superposed coherent states, *Phys. Lett. A* **358**, 115 (2006).
- [13] S. L. Braunstein and P. van Loock, Quantum information with continuous variables, *Rev. Mod. Phys.* **77**, 513 (2005).
- [14] H. Jeong, M. S. Kim, and J. Lee, Quantum-information processing for a coherent superposition state via a mixed entangled coherent channel, *Phys. Rev. A* **64**, 052308 (2001).
- [15] A. Gilchrist, K. Nemoto, W. J. Munro, T. C. Ralph, S. Glancy, S. L. Braunstein, and G. J. Milburn, Schrödinger cats and their power for quantum information processing, *J. Opt. B: Quantum Semiclass. Opt.* **6**, S828 (2004).
- [16] B. Vlastakis, G. Kirchmair, Z. Leghtas, S. E. Nigg, L. Frunzio, S. M. Girvin, M. Mirrahimi, M. H. Devoret, and R. J. Schoelkopf, Deterministically Encoding Quantum Information Using 100-Photon Schrödinger Cat States, *Science* **342**, 607 (2013).
- [17] P. T. Cochrane, G. J. Milburn, and W. J. Munro, Macroscopically distinct quantum-superposition states as a bosonic code for amplitude damping, *Phys. Rev. A* **59**, 2631 (1999).
- [18] H. Jeong and M. S. Kim, Efficient quantum computation using coherent states, *Phys. Rev. A* **65**, 042305 (2002).
- [19] T. C. Ralph, A. Gilchrist, G. J. Milburn, W. J. Munro, and S. Glancy, Quantum computation with optical coherent states, *Phys. Rev. A* **68**, 042319 (2003).
- [20] M. Mirrahimi, Z. Leghtas, V. V. Albert, S. Touzard, R. J. Schoelkopf, L. Jiang, and M. H. Devoret, Dynamically protected cat-qubits: A new paradigm for universal quantum computation, *New J. Phys.* **16**, 045014 (2014).
- [21] N. Ofek, A. Petrenko, R. Heeres, P. Reinhold, Z. Leghtas, B. Vlastakis, Y. Liu, L. Frunzio, S. M. Girvin, L. Jiang, M. Mirrahimi, M. H. Devoret, and R. J. Schoelkopf, Extending the lifetime of a quantum bit with error correction in superconducting circuits, *Nature (London)* **536**, 441 (2016).
- [22] J. Guillaud, J. Cohen, and M. Mirrahimi, Quantum computation with cat qubits, *SciPost Phys. Lect. Not.* **72**, 72 (2023).
- [23] W. J. Munro, K. Nemoto, G. J. Milburn, and S. L. Braunstein, Weak-force detection with superposed coherent states, *Phys. Rev. A* **66**, 023819 (2002).
- [24] J. Joo, W. J. Munro, and T. P. Spiller, Quantum Metrology with Entangled Coherent States, *Phys. Rev. Lett.* **107**, 083601 (2011).
- [25] M. Bild, M. Fadel, Y. Yang, U. Von Lüpke, P. Martin, A. Bruno, and Y. Chu, Schrödinger cat states of a 16-microgram mechanical oscillator, *Science* **380**, 274 (2023).
- [26] M. Brune, S. Haroche, J. M. Raimond, L. Davidovich, and N. Zagury, Manipulation of photons in a cavity by dispersive atom-field coupling: Quantum-nondemolition measurements and generation of “Schrödinger cat” states, *Phys. Rev. A* **45**, 5193 (1992).
- [27] G. C. Guo and S. B. Zheng, Generation of Schrödinger cat states via the Jaynes-Cummings model with large detuning, *Phys. Lett. A* **223**, 332 (1996).
- [28] C. Monroe, D. M. Meekhof, B. E. King, and D. J. Wineland, A “Schrödinger Cat” Superposition State of an Atom, *Science* **272**, 1131 (1996).
- [29] S. Bose, K. Jacobs, and P. L. Knight, Preparation of nonclassical states in cavities with a moving mirror, *Phys. Rev. A* **56**, 4175 (1997).
- [30] A. D. Armour, M. P. Blencowe, and K. C. Schwab, Entanglement and Decoherence of a Micromechanical Resonator Via Coupling to a Cooper-Pair Box, *Phys. Rev. Lett.* **88**, 148301 (2002).
- [31] S. Ashhab and F. Nori, Qubit-oscillator systems in the ultrastrong-coupling regime and their potential for preparing nonclassical states, *Phys. Rev. A* **81**, 042311 (2010).
- [32] J.-Q. Liao and L. Tian, Macroscopic Quantum Superposition in Cavity Optomechanics, *Phys. Rev. Lett.* **116**, 163602 (2016).
- [33] J.-Q. Liao, J.-F. Huang, and L. Tian, Generation of macroscopic Schrödinger-cat states in qubit-oscillator systems, *Phys. Rev. A* **93**, 033853 (2016).
- [34] Y.-H. Chen, W. Qin, X. Wang, A. Miranowicz, and F. Nori, Shortcuts to Adiabaticity for the Quantum Rabi Model: Efficient Generation of Giant Entangled Cat States via Parametric Amplification, *Phys. Rev. Lett.* **126**, 023602 (2021).
- [35] A. Ourjoumtsev, R. Tualle-Brouri, J. Laurat, and P. Grangier, Generating Optical Schrödinger Kittens for Quantum Information Processing, *Science* **312**, 83 (2006).
- [36] A. Ourjoumtsev, H. Jeong, R. Tualle-Brouri, and P. Grangier, Generation of optical ‘Schrödinger cats’ from photon number states, *Nature (London)* **448**, 784 (2007).
- [37] H. Takahashi, K. Wakui, S. Suzuki, M. Takeoka, K. Hayasaka, A. Furusawa, and M. Sasaki, Generation of Large-Amplitude Coherent-State Superposition Via Ancilla-Assisted Photon Subtraction, *Phys. Rev. Lett.* **101**, 233605 (2008).
- [38] F. X. Sun, S. S. Zheng, Y. Xiao, Q. Gong, Q. He, and K. Xia, Remote Generation of Magnon Schrödinger Cat State via Magnon-Photon Entanglement, *Phys. Rev. Lett.* **127**, 087203 (2021).
- [39] D.-L. Hu, J.-J. Zou, F.-X. Sun, J.-Q. Liao, Q. He, and Z.-L. Xiang, Fast generation of high-fidelity mechanical non-Gaussian states via additional amplifier and photon subtraction, *Phys. Rev. Res.* **5**, L032031 (2023).
- [40] D. M. Han, F. X. Sun, N. Wang, Y. Xiang, M. H. Wang,

- M. S. Tian, Q. He, and X. L. Su, Remote Preparation of Optical Cat States Based on Gaussian Entanglement, *Laser Photon. Rev.* **17**, 2300103 (2023).
- [41] U. B. Hoff, J. Kollath-Bönig, J. S. Neergaard-Nielsen, and U. L. Andersen, Measurement-Induced Macroscopic Superposition States in Cavity Optomechanics, *Phys. Rev. Lett.* **117**, 143601 (2016).
- [42] R. Y. Teh, S. Kiesewetter, P. D. Drummond, and M. D. Reid, Creation, storage, and retrieval of an optomechanical cat state, *Phys. Rev. A* **98**, 063814 (2018).
- [43] A. Miranowicz, R. Tanas, and S. Kielich, Generation of discrete superpositions of coherent states in the anharmonic oscillator model, *Quantum Opt.* **2**, 253 (1990).
- [44] L.-M. Kuang and L. Zhou, Generation of atom-photon entangled states in atomic Bose-Einstein condensate via electromagnetically induced transparency, *Phys. Rev. A* **68**, 043606 (2003).
- [45] J. Q. Liao, J. F. Huang, L. Tian, L. M. Kuang, and C. P. Sun, Generalized ultrastrong optomechanical-like coupling, *Phys. Rev. A* **101**, 063802 (2020).
- [46] A. Grimm, N. E. Frattini, S. Puri, S. O. Mundhada, S. Touzard, M. Mirrahimi, S. M. Girvin, S. Shankar, and M. H. Devoret, Stabilization and operation of a Kerr-cat qubit, *Nature (London)* **584**, 205 (2020).
- [47] X. L. Yin, Y. H. Zhou, and J. Q. Liao, All-optical quantum simulation of ultrastrong optomechanics, *Phys. Rev. A* **105**, 013504 (2022).
- [48] X. He, Y. Lu, D. Bao, H. Xue, W. Jiang, Z. Wang, A. Roudsari, P. Delsing, J. Tsai, and Z. Lin, Fast generation of Schrödinger cat states using a Kerr-tunable superconducting resonator, *Nat. Commun.* **14**, 6358 (2023).
- [49] J. F. Poyatos, J. I. Cirac, and P. Zoller, Quantum Reservoir Engineering with Laser Cooled Trapped Ions, *Phys. Rev. Lett.* **77**, 4728 (1996).
- [50] M. Asjad and D. Vitali, Reservoir engineering of a mechanical resonator: generating a macroscopic superposition state and monitoring its decoherence, *J. Phys. B: At. Mol. Opt. Phys.* **47**, 045502 (2014).
- [51] M. Brunelli, O. Houhou, D. W. Moore, A. Nunnenkamp, M. Paternostro, and A. Ferraro, Unconditional preparation of nonclassical states via linear-and-quadratic optomechanics, *Phys. Rev. A* **98**, 063801 (2018).
- [52] P. Lodahl, S. Mahmoodian, S. Stobbe, A. Rauschenbeutel, P. Schneeweiss, J. Volz, H. Pichler, and P. Zoller, Chiral quantum optics, *Nature (London)* **541**, 473 (2017).
- [53] L. Feng, M. Ayache, J. Huang, Y.-L. Xu, M.-H. Lu, Y.-F. Chen, Y. Fainman, and A. Scherer, Nonreciprocal Light Propagation in a Silicon Photonic Circuit, *Science* **333**, 729 (2011).
- [54] M. Scheucher, A. Hilico, E. Will, J. Volz, and A. Rauschenbeutel, Quantum optical circulator controlled by a single chirally coupled atom, *Science* **354**, 1577 (2016).
- [55] D. L. Sounas and A. Alù, Non-reciprocal photonics based on time modulation, *Nat. Photon.* **11**, 774 (2017).
- [56] L. Tang, J. Tang, M. Chen, F. Nori, M. Xiao, and K. Xia, Quantum Squeezing Induced Optical Nonreciprocity, *Phys. Rev. Lett.* **128**, 083604 (2022).
- [57] Y.-L. Zuo, Y.-F. Jiao, X.-W. Xu, A. Miranowicz, L.-M. Kuang, and H. Jing, Chiral photon blockade in the spinning Kerr resonator, *Opt. Express* **32**, 22020 (2024).
- [58] B. M. Terhal, Quantum error correction for quantum memories, *Rev. Mod. Phys.* **87**, 307 (2015).
- [59] I. Georgescu, 25 years of quantum error correction, *Nat. Rev. Phys.* **2**, 519 (2020).
- [60] A. Metelmann and A. A. Clerk, Nonreciprocal Photon Transmission and Amplification via Reservoir Engineering, *Phys. Rev. X* **5**, 021025 (2015).
- [61] P. Yang, X. Xia, H. He, S. Li, X. Han, P. Zhang, G. Li, P. Zhang, J. Xu, Y. Yang, and T. Zhang, Realization of Nonlinear Optical Nonreciprocity on a Few-Photon Level Based on Atoms Strongly Coupled to an Asymmetric Cavity, *Phys. Rev. Lett.* **123**, 233604 (2019).
- [62] Y. F. Jiao, S. D. Zhang, Y. L. Zhang, A. Miranowicz, L. M. Kuang, and H. Jing, Nonreciprocal Optomechanical Entanglement against Backscattering Losses, *Phys. Rev. Lett.* **125**, 143605 (2020).
- [63] X. W. Xu, Y. Li, B. Li, H. Jing, and A. X. Chen, Nonreciprocity via Nonlinearity and Synthetic Magnetism, *Phys. Rev. Appl.* **13**, 044070 (2020).
- [64] M. X. Dong, K. Y. Xia, W. H. Zhang, Y. C. Yu, Y. H. Ye, E. Z. Li, L. Zeng, D. S. Ding, B. S. Shi, G. C. Guo, and F. Nori, All-optical reversible single-photon isolation at room temperature, *Sci. Adv.* **7**, eabe8924 (2021).
- [65] M. Fruchart, R. Hanai, P. B. Littlewood, and V. Vitelli, Nonreciprocal phase transitions, *Nature (London)* **592**, 363 (2021).
- [66] Y. Xu, J. Y. Liu, W. Liu, and Y. F. Xiao, Nonreciprocal phonon laser in a spinning microwave magnomechanical system, *Phys. Rev. A* **103**, 053501 (2021).
- [67] G. B. Malykin, The Sagnac effect: Correct and incorrect explanations, *Phys. Usp.* **43**, 1229 (2000).
- [68] S. Maayani, R. Dahan, Y. Kligerman, E. Moses, A. U. Hassan, H. Jing, F. Nori, D. N. Christodoulides, and T. Carmon, Flying couplers above spinning resonators generate irreversible refraction, *Nature (London)* **558**, 569 (2018).
- [69] H. Jing, H. Lü, S. K. Özdemir, T. Carmon, and F. Nori, Nanoparticle sensing with a spinning resonator, *Optica* **5**, 1424 (2018).
- [70] R. Huang, A. Miranowicz, J. Q. Liao, F. Nori, and H. Jing, Nonreciprocal Photon Blockade, *Phys. Rev. Lett.* **121**, 153601 (2018).
- [71] Y. F. Jiao, J. X. Liu, Y. Li, R. Yang, L. M. Kuang, and H. Jing, Nonreciprocal Enhancement of Remote Entanglement between Nonidentical Mechanical Oscillators, *Phys. Rev. Appl.* **18**, 064008 (2022).
- [72] D.-G. Lai, A. Miranowicz, and F. Nori, Nonreciprocal Topological Phonon Transfer Independent of Both Device Mass and Exceptional-Point Encircling Direction, *Phys. Rev. Lett.* **132**, 243602 (2024).
- [73] Z.-H. Li, L.-L. Zheng, Y. Wu, and X.-Y. Lü, Nonreciprocal generation of Schrödinger cat state induced by topology, *Sci. China Phys. Mech. Astron.* **64**, 240313 (2024).
- [74] W. P. Schleich, *Quantum Optics in Phase Space* (Wiley VCH, Berlin, 2001).
- [75] H. Fröhlich, Theory of the Superconducting State. I. The Ground State at the Absolute Zero of Temperature, *Phys. Rev.* **79**, 845 (1950).
- [76] S. Nakajima, Perturbation theory in statistical mechanics, *Adv. Phys.* **4**, 363 (1955).
- [77] S. M. Barnett and P. M. Radmore, *Methods in*

- Theoretical Quantum Optics* (Clarendon Press, Oxford, 1997).
- [78] F. A. M. de Oliveira, M. S. Kim, P. L. Knight, and V. Bužek, Properties of displaced number states, *Phys. Rev. A* **41**, 2645 (1990).
- [79] A. V. Kavokin, J. J. Baumberg, G. Malpuech, and F. P. Laussy, *Microcavities* (Oxford University Press, New York, 2017).
- [80] T. Aoki, B. Dayan, E. Wilcut, W. Bowen, A. Parkins, T. Kippenberg, K. Vahala, and H. Kimble, Observation of strong coupling between one atom and a monolithic microresonator, *Nature (London)* **443**, 671 (2006).
- [81] B. Dayan, A. S. Parkins, T. Aoki, E. P. Ostby, K. J. Vahala, and H. J. Kimble, A Photon Turnstile Dynamically Regulated by One Atom, *Science* **319**, 1062 (2008).